Journal of Materials Science: Materials in Medicine (2025)36:28
https://doi.org/10.1007/s10856-025-06874-7

BIOMATERIALS SYNTHESIS AND CHARACTERIZATION

Original Research

Self-assembled injectable Icariin@ Ti_3C_2Tx/doxorubicin hydrogel preserving osteogenesis while synergizing photodynamic and chemodynamic therapy for osteosarcoma

Jiahao Fu[1,2] · Hao Chen[1,2] · Yiqiao Zhao[3] · Hongzhong Xi[1,2] · Yixuan Huang[1,2] · Chenglin Liu[1,2] · Yaokun Wu[1,2] · Wei Song[1,2] · Xin Liu[1,2] · Bin Du[1,2] · Guangquan Sun[1,2]

Received: 29 November 2024 / Accepted: 20 February 2025

Abstract

Local therapy involving injectable hydrogel systems loaded with doxorubicin (DOX) has garnered significant attention in the realm of osteosarcoma (OS) research. Nevertheless, it has been noted that the local delivery of high-dose DOX exerts a pronounced inhibitory impact on osteogenesis, which is detrimental to the restoration of functional capabilities after OS treatment. To address this challenge, we have designed a self-assembled injectable hydrogel system that integrates photodynamic and chemodynamic therapy, aiming to enhance efficacy while mitigating adverse effects on osteogenic differentiation. In this study, an injectable sodium alginate (SA) hydrogel was fabricated by encapsulating titanium carbide powder (Ti_3C_2Tx) and osteoprotegerin Icariin (ICA) along with DOX. This hydrogel system demonstrated remarkable drug-loading capacity and sustained drug release. Furthermore, under near-infrared (NIR) irradiation, the hydrogel displayed outstanding photothermal effects, which, in conjunction with chemotherapy and phototherapy, effectively eradicated UMR-106 tumor cells in vitro. The incorporation of ICA not only enhanced the anti-tumor effect but also alleviated the adverse effects of DOX on the osteogenic differentiation inhibition of bone marrow mesenchymal stem cells (BMSCs). In vivo, findings further confirmed that injectable ITD/SA hydrogels can synergistically heighten anti-osteosarcoma effectiveness while mitigating local osteogenic toxicity. Given these benefits, this hydrogel holds extensive application prospects in the local therapy of OS.

Graphical Abstract

Schematic diagram of injectable NIR-responsive ITD/SA hydrogel phototherapy versus chemotherapy for OS and protection against BMSCS. (A) Illustration of the preparation process of the ITD/SA hydrogel. (B) Schematic of the therapeutic effect of ITD/SA under NIR irradiation.

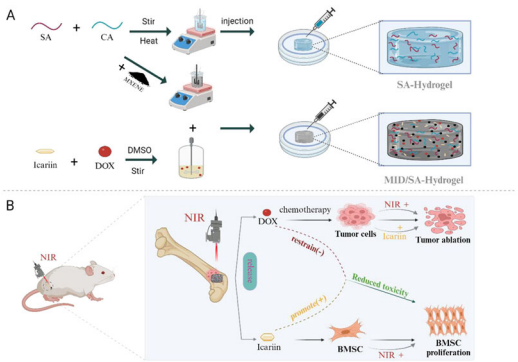

✉ Xin Liu
liuxinsurg@163.com

✉ Bin Du
fsyy00608@njucm.edu.cn

✉ Guangquan Sun
sunguangquan1981@163.com

[1] Affiliated Hospital of Nanjing University of Chinese Medicine, Nanjing, Jiangsu, China

[2] Department of Orthopaedics, Jiangsu Provincial Hospital of Traditional Chinese Medicine, Nanjing, Jiangsu, China

[3] School of Chemistry and Chemical Engineering, Nanjing University of Science and Technology, Nanjing, Jiangsu, China

Published online: 15 March 2025

1 Introduction

Osteosarcoma (OS) is a highly aggressive primary malignant bone tumor associated with frequent metastasis, particularly afflicting children and adolescents [1, 2]. In clinical practice, chemotherapy combined with radiotherapy remains the standard treatment strategy for OS [3]. Doxorubicin (DOX), a first-line chemotherapeutic agent for OS, is limited by its severe systemic toxicity during long-term administration, including dose-dependent cardiotoxicity, myelosuppression, and impaired osteogenesis [4, 5]. These limitations arise primarily from the drug's off-target biodistribution, leading to subtherapeutic concentrations within tumor tissues while causing collateral damage to healthy organs [6]. To address these challenges, the design of a localized drug delivery system has emerged as a critical priority. These systems would enhance drug utilization efficiency, minimize the toxic side effects of chemotherapeutic agents on the body, and potentiate the anti-tumor effects.

Photothermal therapy (PTT) has emerged as a promising non-invasive therapeutic modality that has gained significant attention due to its low cost and high targeting specificity [7, 8]. The activation of photothermal conversion agents with near-infrared (NIR) enables PTT to harness their thermal effects, thereby facilitating the ablation of tumor lesions through a local, non-invasive approach to tumor treatment [9, 10]. The intensity of the PTT light can be adjusted to meet specific therapeutic requirements, thereby offering greater biosafety and a lower risk of tissue damage [11]. At present, a plethora of photothermal conversion materials, including gold nanoparticles, carbon nanotubes, transition metal carbides or nitrides, black phosphorus, and polydopamine, have been subjected to extensive investigation and have been employed in the context of cancer treatment [12–14]. An additional feature of the PTT system is that the controlled release of drugs encapsulated within it can be precisely regulated following localized heating. In recent years, the combination of chemotherapy and PTT has emerged as a promising approach in the field of oncology [15]. For example, Li et al. Who developed an injectable black phosphorus nanosheet (BPNS)/DOX/chitosan (CS) hydrogel that integrates PTT with chemotherapy [16]. Under NIR irradiation, the hydrogel system generates photothermal effects that, combined with the localized sustained release of DOX, demonstrate superior cancer cell eradication efficacy compared to monotherapies. Moreover, the hydrogel displays notable plasticity and drug-loading capacity to encapsulate BPNS for prolonged sustained release, thereby promoting osteogenesis. Consequently, it has been demonstrated to eradicate cancerous cells effectively. Nevertheless, the system remains imperfect, exhibiting shortcomings such as suboptimal environmental stability, elevated production costs, and vulnerability to oxidation of BPNS [17, 18]. Additionally, the intricate preparation and limited solubility of CS hydrogels, along with the potential osteogenic suppression caused by DOX, remain unresolved issues.

MXene is a recently discovered two-dimensional material comprising alternating layers of metal ions and carbon-nitrogen units, with a surface area enriched in active sites. This distinctive structure endows MXene with a highly malleable electronic structure and surface charge density [19]. As a kind of MXene, Ti_3C_2Tx has attracted considerable interest due to its near 100% internal photothermal conversion efficiency and excellent biocompatibility [20]. It exhibits superior thermal conversion performance and good chemical stability compared to BPNS. Sodium alginate (SA), a naturally occurring polysaccharide polymer, has gained widespread application in drug delivery systems owing to several advantageous characteristics, including its abundant natural sources, cost-effectiveness, non-toxicity, favorable biocompatibility, and excellent solubility [21, 22]. Citric acid (CA), as a natural organic acid, is characterized by exceptional biosecurity and superior degradability [23]. A straightforward solution mixing method enables CA to form hydrogel bonds with SA, forming a hydrogel with remarkable controlled release properties. This hydrogel exhibits superior sustained release effects in drug delivery systems, offering new avenues for enhancing drug efficacy and mitigating adverse effects.

Icariin (ICA) is a natural flavonol glycoside extracted from Epimedium. It has been demonstrated the ability to reverse multidrug resistance in cancer cells, enhance DOX-induced apoptosis, and effectively inhibit tumor cell proliferation by increasing the retention of DOX within tumor cells, thereby promoting tumor cell apoptosis [24]. Moreover, ICA has been demonstrated to stimulate the proliferation and osteogenic differentiation of bone marrow mesenchymal stem cells (BMSCs), inhibit the bone resorption activity of osteoclasts, and promote matrix calcification, thereby enhancing bone strength [25, 26]. These findings suggest that ICA may provide a degree of protection against the osteogenic inhibition induced by DOX.

Therefore, we propose to develop a self-assembled injectable ICA@ Ti_3C_2Tx /DOX hydrogel system. As illustrated in "Graphical abstract (A)", the interactions between the -OH of SA and the C=O of CA with the -COOH of CA were initially employed to prepare a stable, injectable SA hydrogel three-dimensional network through precise molecular recognition and self-assembly processes. Subsequently, the molecular components, including ICA, DOX, and Ti_3C_2Tx, were accurately encapsulated within the three-dimensional network structure of the SA hydrogel. As illustrated in "Graphical abstract (B)", a schematic of the therapeutic effect of the ITD/SA hydrogel demonstrates that the SA hydrogel encapsulates

Ti_3C_2Tx, DOX, and ICA, thereby forming an injectable sustained-release carrier. As proof of concept, the composite hydrogel demonstrated enhanced therapeutic efficacy and reduced cytotoxicity in in vitro cellular experiments. The release of the drug, in conjunction with the photothermal effect of Ti_3C_2Tx, under NIR irradiation, results in a synergistic enhancement of chemotherapy and phototherapy, thereby enhancing the anti-tumor performance. Notably, the incorporation of ICA mitigates the osteogenic inhibitory effects associated with DOX administration, aiming to achieve enhanced efficacy while concurrently reducing toxicity. In other words, it reduces the chemotherapy-induced osteogenic inhibition while enhancing the anti-tumor effects.

2 Materials and methods

2.1 Materials

The compounds DOX and ICA were obtained from Shenzhen Wanle Pharmaceutical Co., Ltd. SA and CA were acquired from China National Medicine Group Chemical Reagent Co., Ltd., Ti_3C_2Tx (multilayered clay) were bought from Foshan Xinxi Technology Co., Ltd. The mouse embryonic osteoblasts cells MC-3T3, rat BMSCs, and rat osteosarcoma cells UMR-106 were procured from the National Certified Cell Culture Preservation Center (TCR11; Shanghai, China). The following reagents were obtained from Gibco Life Technologies (Grand Island, USA) for in vitro cell culture: fetal bovine serum, Dulbecco's Modified Eagle Medium/Nutrient Mixture F-12 (DMEM/F-12), DMEM medium, 1640 medium. The Cell Counting Kit-8 (CCK-8 assay kit), Calcein/PI Live/Dead Double Staining Kit, Ki67 Cell Proliferation Detection Kit (IF, Green, Mouse mAb), RIPA lysis buffer, BCA protein assay kit, polyvinylidene fluoride (PVDF) membrane, and 4% paraformaldehyde fixing solution were sourced from Beyotime Biotechnology Co., Ltd. (Jiangsu, China). The primary antibodies for PCNA, BCL-2, Caspase-3, and β-actin, as well as the secondary antibodies, were provided by Proteintech (Hubei, China). The HE trichrome staining kits were acquired from Dream Bio Co. (Jiangsu, China).

2.2 Preparation and characterization of ITD/SA

By testing the effects of different hydrogel concentrations on gel formation time and swelling rate, we found (Figs. S2 and S3) that the concentration of 40 mg/mL combines the characteristics of fast sol-gel transition and high swelling rate, so we chose 40 mg/mL as the official experimental concentration. Forty milligrams of SA and an equivalent amount of Ti_3C_2Tx powder were added to 1 mL of ultrapure water. Then, ultrasonic dispersion was performed to form a homogeneous Ti_3C_2Tx/SA solution. Subsequently, a specific quantity of DOX and ICA powders were dissolved in dimethyl sulfoxide (DMSO), while 40 mg of CA was dissolved in 1 mL of ultrapure water. The two solutions were mixed thoroughly at room temperature to form a homogeneous ITD/SA hydrogel system.

The rheological properties of SA, DOX/SA, and ITD/SA hydrogels were evaluated using a rotational rheometer (MCR302). Then, the prepared hydrogels were freeze-dried in a freeze-dryer (LGJ-10C, Beijing Scientific Instrument Co., Ltd.) at −48 °C for 72 h. A scanning electron microscope (SEM, Hitachi Regulus 8100, Japan) was utilized to observe the internal morphology of the hydrogels. Subsequently, the composition and structure of the substances within the drug-loaded hydrogels were analyzed and identified using a Fourier transform infrared spectrometer (ThermoNICOLETIS20). The hydrogel swelling rate was evaluated through a direct measurement method to assess the hydrogel drug-carrying capacity. This involved weighing freeze-dried SA, DOX/SA, and ITD/SA hydrogels with a diameter of 12 mm and a height of 10 mm (initial mass was noted as M0), and then immersing them at 37 °C in 20 mL of phosphate buffer solution (PBS, pH = 7.4). At the designated time, the hydrogels were removed and reweighed (recorded as Mt). The hydrogel's water absorption (W) was calculated under the following formula(1).

$$W = \frac{\mathrm{Mt} - \mathrm{M0}}{\mathrm{M0x100}}\% \quad (1)$$

2.3 In vitro drug release

To evaluate the in vitro drug release ability of the hydrogels, the ITD/SA hydrogels were divided into four groups. Additionally, TD/SA hydrogels were prepared for comparison. Following complete solidification of the hydrogels, 5 mL of simulated body fluid (SBF) solution was added to each centrifuge tube, which was then placed in a constant temperature oscillating incubator at 37 °C and shaken at 70 rpm. Two ITD/SA hydrogels were subjected to NIR (temperature maintained at 42 ± 0.5 °C) for 5 min, except the others. The supernatant was aspirated and replenished at predetermined times with an equal volume of SBF solution. Subsequently, the absorbance of the supernatant at 485 and 450 nm was determined using a UV-visible spectrophotometer, allowing the calculation of the amount of drug released from DOX and ICA. Furthermore, the release standard curves of DOX and ICA in pure water were determined, and the cumulative drug release (C) was calculated using formula (2)

$$\mathrm{C} = (n/N)\mathrm{x}100\% \quad (2)$$

C: cumulative drug release; *n*: drug release amount at a specified time; *N* Total amount of drug.

2.4 In vitro photothermal effect

The photothermal performance of Ti_3C_2Tx at varying concentrations, molded SA, DOX/SA, TD/SA, and ITD/SA hydrogels were tested in vitro using an infrared thermal imaging camera(HIKMICRO K20, China), with SA hydrogels as a control group. Briefly, the above items were loaded into centrifuge tubes and irradiated with NIR (1 W/cm^2, 5 min). Record the temperature change and thermogram.

2.5 In vitro cellular experiments

2.5.1 Cell culture

The MC-3T3, BMSCs, and UMR-106 cells were cultured in the corresponding complete medium, with the medium changed every 2 days. The cells were cultured in a humidified incubator (Jinghong, Shanghai, China) set at 37 °C and 5% CO_2 under standard laboratory practice. The passaging procedure was initiated once the cells had reached 80% to 90% confluence under microscopic observation. The P3 generation of cells was selected for the subsequent in vitro experiments. All experimental items (reagents, hydrogels, and cell culture plate) were subjected to ultraviolet (UV) irradiation for 1 h before utilization.

2.5.2 In vitro cytotoxicity assay

The CCK-8 assay was employed to evaluate the cytotoxicity of biological materials. MC-3T3 cells were seeded in 96-well plates at a density of 5×10^3 cells per well. Subsequently, SA, ICA, Ti_3C_2Tx, and IT/SA were added to the well plates in triplicate and incubated with the cells for 24 and 48 h. At the end of the incubation period, the cells were further incubated with a medium containing CCK-8 solution for 2 h under dark conditions. Subsequently, optical density at 450 nm was measured using a microplate reader(BioTek, USA).

2.5.3 In vitro anti-tumor activity

The in vitro anti-tumor efficacy of ITD/SA hydrogels was assessed by CCK-8 assay and Live/Dead staining using UMR-106 cells. CCK-8 assay was performed as above, with only the cells replaced with UMR-106, and the TD/SA and ITD/SA groups were irradiated with NIR for 5 min (maintained at 42 ± 0.5 °C).

UMR-106 cells were inoculated in 24-well plates at a density of 5×10^4 cells per well and incubated with each hydrogel (50 μL) for 24 and 72 h before staining the cells using the Calcein/PI Live/Dead Double Staining Kit. Calcein-AM and Propidium Iodide (PI) were used to label live and dead cells, respectively. Images of the stained cells were captured using an inverted fluorescence microscope (Olympus, Japan).

2.5.4 Scratch assay

We evaluated the effect of ITD/SA hydrogel on the migration ability of UMR-106 cells through scratch assay. UMR-106 cells were seeded in 6-well plates at a density of 2×10^5 cells/well. After the cells were fused entirely, a blank area was formed by drawing a straight line in each well with a 200 μL gun tip. Subsequently, the corresponding 200 μL of hydrogel was added to each well. The TD/SA and ITD/SA groups were exposed to NIR irradiation. Cell migration progression was observed at 0 and 24 h using an inverted phase contrast microscope (Olympus, Japan), and the cell migration area was calculated using ImageJ software.

2.5.5 Ki67 immunofluorescence staining

UMR-106 cells were co-cultured with 200 μL of hydrogels (SA, DOX/SA, TD/SA, ITD/SA) in 6-well plates at a density of 2×10^5 cells/well for 72 h and then fixed with immunostaining fixative for 15 min at room temperature. They were then incubated with Ki67 mouse monoclonal antibody overnight at 4 °C and anti-mouse 488 antibody for 1 h. The intensity of Ki67 protein expression in UMR-106 cells was observed and captured using an inverted fluorescence microscope, and the fluorescence intensity was quantified using ImageJ software.

2.5.6 Western blot assay

The hydrogels were co-cultured with UMR-106 cells in 6-well plates (2×10^5 cells/well) for 72 h and exposed to NIR (808 nm, 1 W/cm^2) for 5 min (with temperature maintained at 42 ± 0.5 °C) every day. Cells were washed three times with PBS buffer and subsequently lysed using radioimmunoprecipitation assay (RIPA) buffer. The lysates were vortex-mixed thoroughly and incubated with continuous agitation for 20–30 min at 4 °C before ultrasonication (3 × 5 s pulses at 20% amplitude) and centrifugation at 1200 × *g* (4 °C, 10 min). Protein concentration was determined using the BCA Protein Assay Kit, and the proteins to be analyzed were then separated by 10% SDS polyacrylamide gel electrophoresis and transferred to a PVDF membrane. The membrane was then blocked with 5% skimmed milk for 2 h and incubated overnight at 4 °C with primary antibodies PCNA (1:5000), BCL-2 (1:1000),

Caspase-3 (1:1000) and β-actin (1:10000). The next day, the membranes were washed with TBST and incubated with corresponding secondary antibodies (1:5000). Finally, the target protein bands were detected and analyzed using a chemiluminescence image analyzer (BIO-RAD, USA), and the protein content was quantified using ImageJ software.

2.5.7 Detoxification effect of ITD/SA

The effects of SA, DOX/SA, TD/SA, and ITD/SA hydrogels on the survival of BMSCs were evaluated using the CCK-8 assay and Live/Dead staining. The specific experimental steps were referred to the CCK-8 assay and Live/Dead staining assay mentioned above, and only the cells were changed to BMSCs and treated similarly.

2.5.8 Osteogenic differentiation of BMSCs

The osteogenic differentiation potential of BMSCs treated with ITD/SA hydrogels was evaluated through alkaline phosphatase (ALP) and alizarin red S (ARS) staining assays. BMSCs were cultured in 24-well plates, and the corresponding hydrogels were added when the cell coverage reached 60%. The original medium was then replaced with an osteogenic induction medium (containing 50 mg/L ascorbic acid, 10 mmol β-phosphoglycerol, and 100 nM dexamethasone). Daily NIR irradiation (5 min, temperature maintained at 42 ± 0.5 °C) was applied to the TD/SA and ITD/SA groups during the incubation process. ALP staining and ARS staining were performed at 7 d and 14 d of culture, respectively, to assess the mineralization effect and the protective effect of ICA against DOX-induced osteogenic inhibition. On day 7 of culture, ALP working solution was prepared using BCIP/NBT ALP Staining Kit (Beyotime, China) according to the instructions of the reagent manufacturer, and the cells were fixed with 4% paraformaldehyde, then stained with the working solution (200 μL/well) for 30 min under dark conditions. When cultured for 14 days, the cells were fixed with paraformaldehyde and then stained with the ARS working solution (200 μL/well) prepared with the Osteogenesis Assay Kit (Beyotime, China) for 30 min at room temperature to quantify calcium deposition.

To further evaluate the protective mechanism of ITD/SA hydrogel during osteogenesis in BMSCs, we examined the expression of relevant osteogenic proteins bone morphogenetic protein 2 (BMP-2) and Runt-related transcription factor 2 (Runx-2) in BMSCs after 3 days of co-culture. BMSCs were co-cultured with hydrogels and treated with NIR every day. After 72 h of culture, a monoclonal antibody to BMP-2 was added and incubated overnight at 4 °C. The cells were then incubated with Cy3-labeled goat anti-rabbit IgG (H + L) for another 1 h at room temperature. Finally, the nuclei of BMSCs were stained with DAPI. The Runx-2 antibody was detected similarly, except the secondary antibody was changed to FITC-labeled goat anti-rabbit IgG (H + L). Images of stained cells were taken using an inverted fluorescence microscope.

The protein expression levels of BMP-2 and Runx-2 in hydrogel-treated BMSCs were assessed by WB assay. The experimental procedures were the same as those described previously for WB assays of tumor-associated proteins, except that BMSCs were used instead of cells, and specific primary and secondary antibodies for BMP-2 (1:200) and Runx-2 (1:200) were used. The results of the experiments were displayed using a chemiluminescent image analyzer and the protein content was quantified.

2.6 In vivo anti-tumor effects

The animal experiments followed the ethical guidelines of the Affiliated Hospital of Nanjing University of Traditional Chinese Medicine (Registration No. 2024NL-KS0173) SPF grade 4-week-old male SD rats were purchased from Nanjing Qinglongshan Animal Centre, and housed in the room with the temperature of 24–26 °C and a regular day-night cycle. Osteosarcoma models were established using the SD rat in situ tumor establishment method [27]. Briefly, after anesthetizing all rats with isoflurane, a 3-cm-long skin incision was made on the lateral side of the left femur, and the periosteum was peeled off. A drill was used to create a 3-mm defect in the coronal direction of the femoral diaphysis and implant 200 μL of UMR-106 cell suspension at a concentration of 1×10^7cells/mL. When tumor volume reached 3 cm^3, the rats were randomly divided into four groups: SA, DOX/SA, TD/SA, and ITD/SA groups, and then the corresponding hydrogels were injected around the tumor. This time point was recorded as day 0, marking the beginning of the 14-day treatment period. The rats were irradiated with NIR for 5 min (temperature maintaining 42 ± 0.5 °C) every other day. The rats' tumor size and body weight were recorded every 2 days throughout the feeding period. Tumor size was then measured based on ellipsoidal volumetry [28]. Tumor volume was calculated using the formula $V = (L \times W^2)/2$, where L represents the diameter of the tumor and W denotes the width.

2.7 Histological analysis

After decalcification of the bone tissue specimens in a 10% EDTA solution for 6 weeks, they were dehydrated in ethanol and embedded in paraffin. They were then cut into 5 μm thick sections and stained with HE. The stained areas were digitally recorded using a Nikon optical microscope.

2.8 Statistical analysis

All data are presented as the mean ± standard deviation (SD). One-way ANOVA was used for multiple comparisons, and t-tests were employed to determine differences between the two groups. Statistical analysis was performed using GraphPad Prism software (version 9.0, USA). In the interpretation of results, $*P < 0.05$, $**P < 0.01$, and $***P < 0.001$ were considered significant, while $*P > 0.05$ was considered not statistically significant.

3 Results

3.1 Characterization of SA, TD, and ITD hydrogels

As shown in Fig. 1A, C, when left at room temperature, the SA hydrogel achieved the sol-gel transition within 360 s, forming a transparent, textured hydrogel. The transition times for the pink DOX/SA hydrogel and the black textured ITD/SA hydrogel were observed within 250 s and 160 s, respectively. A comparison of the three hydrogels suggests that the observed color change was due to the homogeneous doping of the drug, which resulted in the corresponding color presentation. Similarly, the incorporation of the drug with Ti_3C_2Tx resulted in a reduction in the gelation time of the hydrogels. Furthermore, as illustrated in Fig. 1B, these three hydrogels were injectable, thus enabling the local delivery of the drug with Ti_3C_2Tx to the tumor site via a syringe.

The internal structure of the hydrogels after freeze-drying was observed by SEM, as presented in Fig. 2A. The blank hydrogels displayed a three-dimensional network structure with a porous structure of several hundred micrometers in size. Notably, the incorporation of DOX, Ti_3C_2Tx, and ICA, did not induce significant structural modifications to the 3D network structure, indicating that introducing these components does not influence the phase separation behavior of the hydrogel. To gain further insight into the chemical structures of the composite hydrogels, we conducted FTIR characterization of the relevant substances, as Fig. 2B. In the spectrum of SA, the characteristic absorption peaks at 1610 cm^{-1} and 1417 cm^{-1} correspond to the asymmetric and symmetric telescoping vibrations of the COO- and CH groups, respectively. The peak at 1032 cm^{-1} is attributed to the C–O single bond stretching vibration. The C–C single bond backbone vibration is represented by the peak at 1610 cm^{-1}, while the C=O stretching vibration forms a strong absorption peak at 1729 cm^{-1} for CA. The C–O single bond stretching vibration appears at 1209 cm^{-1}. The absorption peaks at 1729 and 1710 cm^{-1} represent the C=O stretching vibration of the -COOH group, while the 1221 and 1209 cm^{-1} peaks represent the C–O stretching vibration of the -COOH groups. The variation of the peaks at 1729–1710 cm^{-1} versus 1221–1209 cm^{-1} indicates the formation of hydrogen bonds during the hydrogel gelation process, which contributes to the formation of the multi-dimensional network structure of the hydrogel. The infrared spectra of the DOX show that the stretching vibrations of the O–H and N–H groups at 3200 cm^{-1} give rise to broad absorption peaks, as do the vibration of the C–C single bond backbone at 1080 cm^{-1} and the stretching vibration of the C–O single bond at 1020 cm^{-1}. The characteristic peaks of the ICA were observed at 2923, 1595, and 1259 cm^{-1}, which correspond to the CH_2 group, benzene ring, and O–CH_3 group, respectively. The observation of the characteristic peaks of DOX and ICA in the ITD/SA hydrogel confirmed the successful preparation of the ITD/SA hydrogel.

As shown in Fig. 2C, the hydrogels reached a swelling equilibrium state after ~72 h of drying. The swelling ratio of the SA, DOX/SA, and ITD/SA hydrogel could reach ~1180%, 1096%, and 1016%, respectively. These results demonstrate that the SA hydrogel has a high drug-loading capacity and the incorporation of drugs has a minimal impact on the swelling rate of the hydrogel, thereby offering a stable carrier platform for the sustained release of drugs.

3.2 In vitro drug release capacity

The sustained drug release ability of ITD/SA composite hydrogels was evaluated using an in vitro drug release assay. As diagramed in Figs. 2D and S1, we obtained the standard drug release curves from DOX and ICA. The 16-day drug release was shown in Fig. 2E, and both showed a consistent and sustained release trend, which entered a plateau period after about 10 days. A comparison of DOX release from TD/SA and ITD/SA hydrogels indicated that the release trends were comparable, suggesting that the addition of ICA did not affect the release rate of DOX. In addition, the change in photothermal factor showed that the drug release rate increased by about 10% under NIR irradiation. This implies that NIR can promote drug release from hydrogels without affecting the long-term release pattern. This phenomenon could be attributed to the photothermal properties of Ti_3C_2Tx, which may lead to heat build-up within the hydrogel, thereby accelerating the degradation of the hydrogel matrix and promoting drug diffusion. These findings suggest the ITD/SA hydrogel system allows for a rapid and effective therapeutic response.

3.3 In vitro photothermal effect

Using an infrared thermography camera, we first monitored the temperature elevation of Ti_3C_2Tx at different

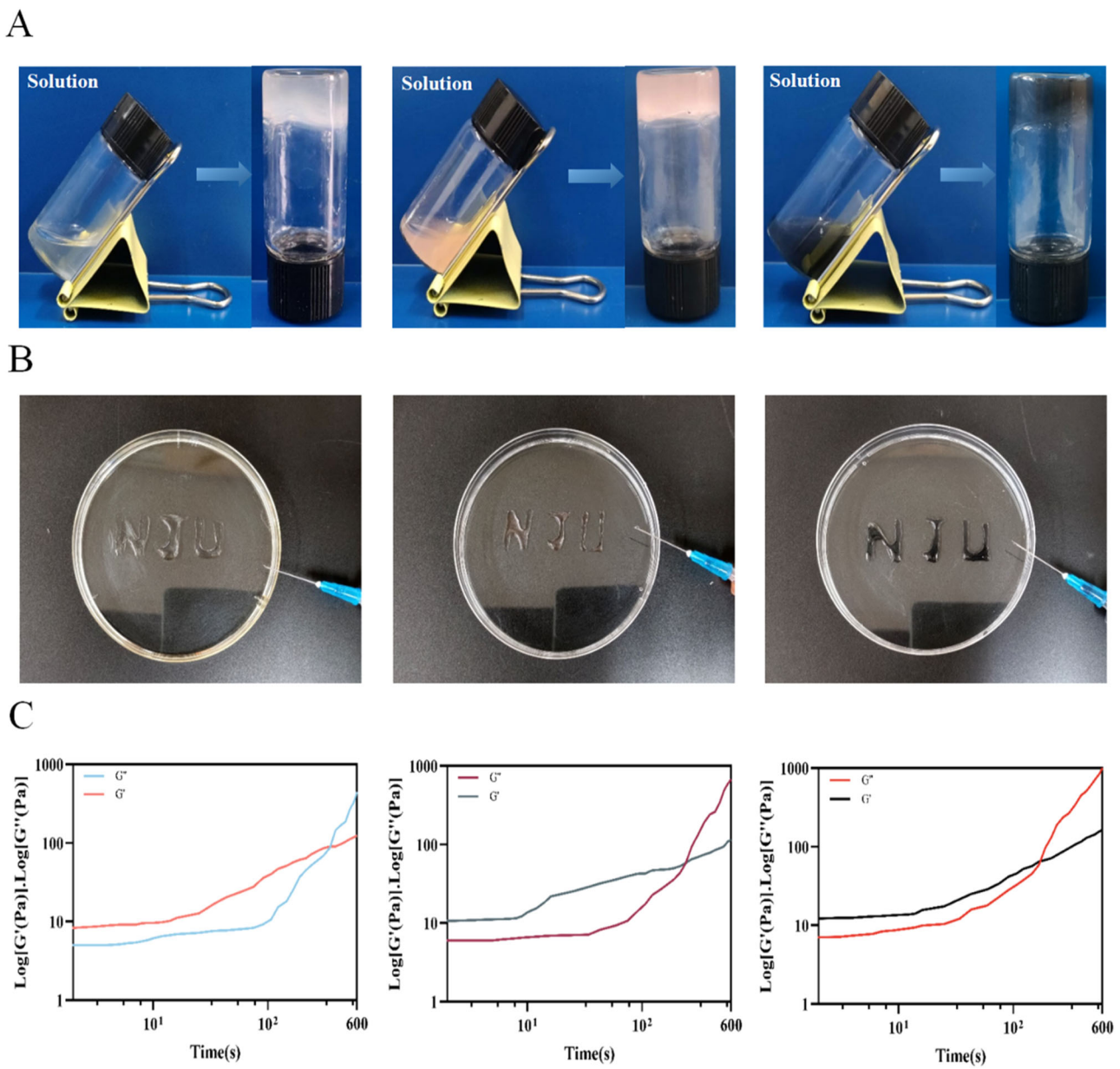

Fig. 1 Characterization of hydrogels. **A** The transition from sol-gel for SA, DOX/SA, and ITD/SA hydrogels. **B** Assessing the injectability of the hydrogels. **C** A Log-Log plot depicting the time-dependent rheological properties of SA, DOX/SA, and ITD/SA hydrogels

concentrations in the NIR for 6 min. As illustrated in Fig. 2F, the temperature of the 25 ppm Ti_3C_2Tx solution increased from 19.3 °C to 48 °C, and the temperature of the 200 ppm Ti_3C_2Tx solution increased from 18.2 °C to 67 °C. This result reveals that Ti_3C_2Tx has excellent photothermal conversion efficiency. Secondly, the photothermal effect of the hydrogel is shown in Fig. 3A, B. After 6 min of irradiation, the temperature changes of the SA and DOX/SA groups were minimal. In contrast, the temperatures of the TD/SA and ITD/SA hydrogels increased by 37.9 °C and 36 °C, respectively, and the temperature of the ITD/SA hydrogel finally reached 52 °C. The difference in the temperature change with Ti_3C_2Tx suggests that encapsulating Ti_3C_2Tx in hydrogels can reduce thermal diffusion, thus prolonging the duration of the photothermal effect and enhancing the photothermal treatment effect. Five consecutive cycles of NIR irradiation were performed on the ITD/SA hydrogel, further evaluating its stability for PTT. As Fig. 3C, after 5 consecutive cycles of on-off NIR irradiation, the temperature trend of the hydrogel remained consistent, indicating that the ITD/SA hydrogel can provide stable photothermal treatment effects and is an excellent antitumor photothermal material.

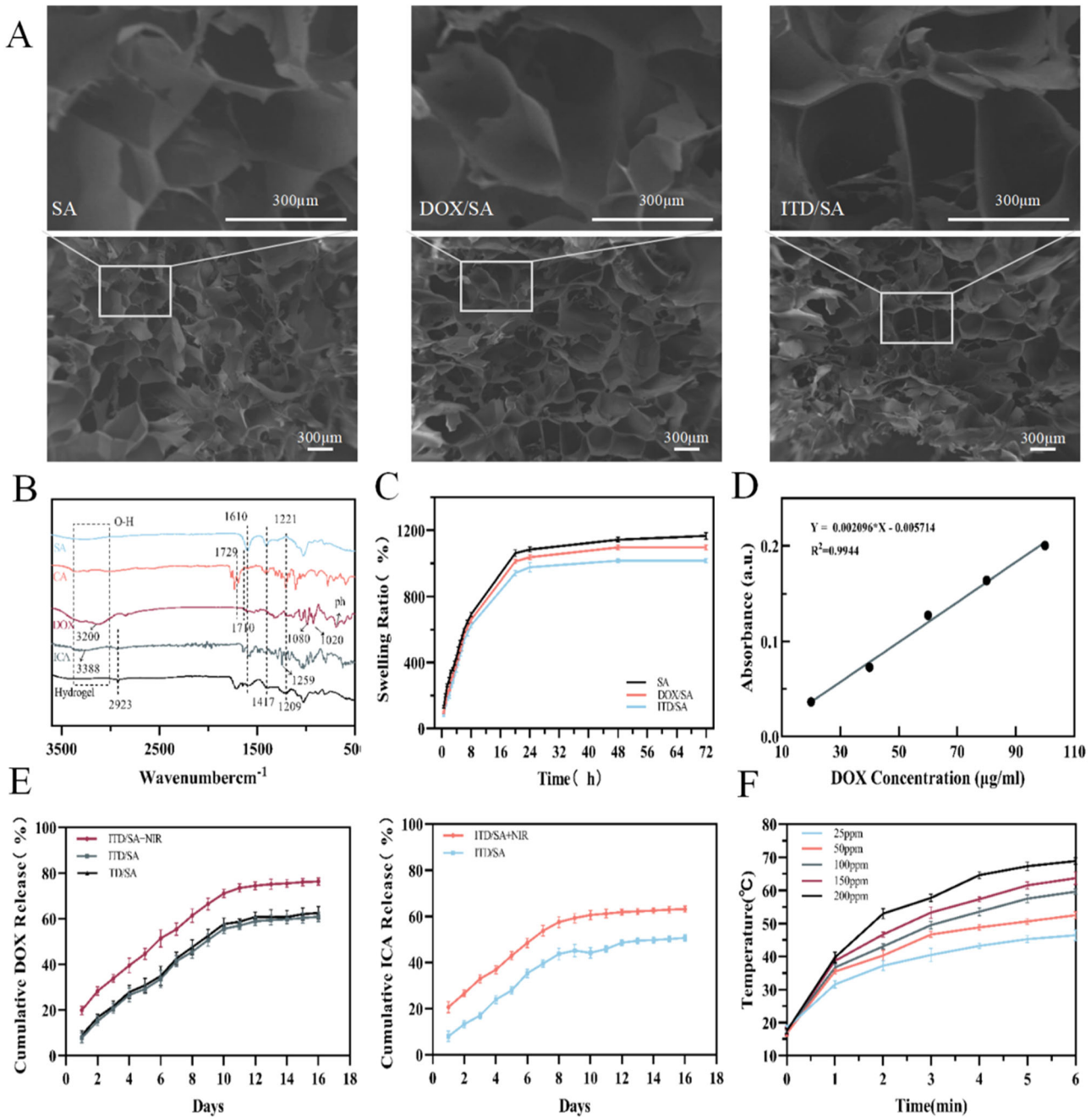

Fig. 2 Characterization of hydrogels. **A** SEM images of SA, DOX/SA, and ITD/SA hydrogels. **B** NIR spectrum of the ITD/SA hydrogel. **C** Swelling ratios of various hydrogel groups. **D** Standard curve of DOX release. **E** Cumulative release curves of DOX and ICA from TD/SA and ITD/SA hydrogels. **F** Photothermal effect curves of different concentrations of Ti_3C_2Tx (25, 50, 100, 150, 200 ppm) under NIR irradiation (808 nm, 1 W/cm^2) for 6 min

3.4 In vitro cytotoxicity assay

Initial cytotoxicity screening of SA hydrogels at varying concentrations was conducted on MC-3T3 and UMR-106 cell lines through preliminary experiments (Figs. S4 and S5). The biocompatibility assessment revealed that concentrations below 100 mg/mL maintained cell viability above 85% in both cell types, demonstrating no significant cytotoxic effects. Comparative analysis of MC-3T3 proliferation rates at 24 h intervals showed that 40 mg/mL SA hydrogel may exhibit enhanced cytocompatibility potential compared to 20 mg/mL concentration, as evidenced by differential proliferation patterns observed on day 2. Notably, both concentrations demonstrated comparable viability profiles in UMR-106 cells without statistical significance. Based on these

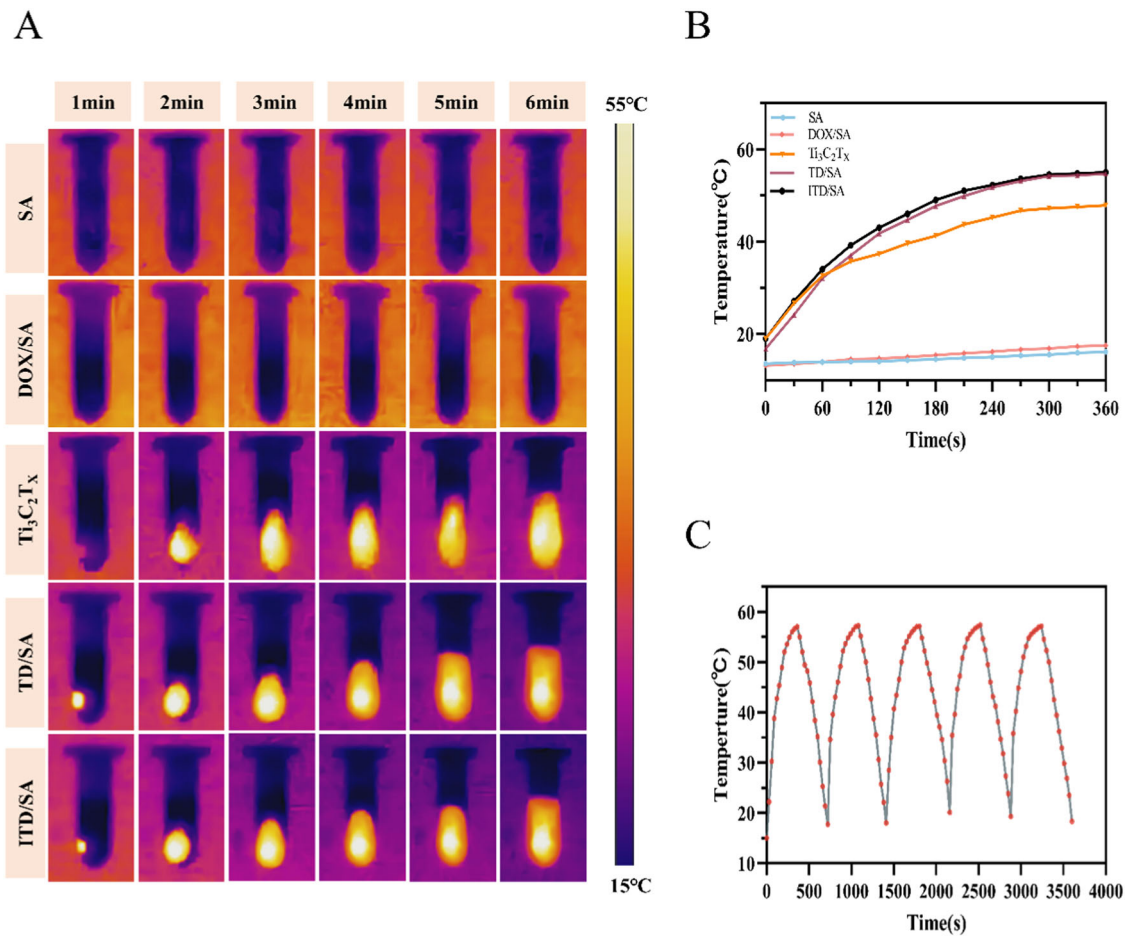

Fig. 3 In vitro photothermal effects. **A** Thermal imaging photographs of SA, DOX/SA, Ti_3C_2Tx, TD/SA, and ITD/SA hydrogels under NIR irradiation (808 nm, 1 W/cm^2) for 6 min. **B** Corresponding photothermal temperature increase curves for the hydrogel groups. **C** Photothermal stability curve of ITD/SA hydrogel under continuous NIR irradiation (808 nm, 1 W/cm^2) for five cycles

findings, the 40 mg/mL SA hydrogel concentration was selected as the optimal formulation for subsequent experimental controls, balancing material performance with biological compatibility requirements. As depicted in Fig. 4A, after co-culturing SA, Ti_3C_2Tx, ICA, and IT/SA materials with cells for 24 h, the cell viability in the SA, ICA, and IT/SA groups all exceeded 103%. After 48 h of incubation, the cell viability in these groups remained above 103%. In contrast, the cell viability of the Ti_3C_2Tx group decreased from 88% to ~79%. In addition, both SA hydrogels and IT/SA hydrogels exhibited good biocompatibility, which may be related to the encapsulation of Ti_3C_2Tx material. A positive indicator for their application in the biomedical field.

3.5 In vitro anti-tumor activity

Similarly, we pre-tested the effect of different concentrations of hydrogel on the survival of UMR-106 cells, and the experimental results are shown in Fig. S5, where we found that the concentration of hydrogel (less than 100 mg/mL) had little effect on the survival of UMR-106 cells. The Live/Dead staining results are presented in Fig. 4D; compared with the SA group, the DOX/SA group exhibited more red fluorescence after 24 and 72 h. Yet, the green fluorescence revealed that a considerable number of cells still survived, potentially attributable to the sustained slow-release effect of its drug, which could not eliminate the tumor rapidly and completely. Instead, the TD/SA and ITD/SA groups displayed a marked increase in red fluorescence after NIR irradiation, confirming significantly enhanced cytotoxic effects on tumor cells. Interestingly, there was little difference in the fluorescence intensity between the two groups after 72 h, which might be related to the photothermal promotion of DOX release. Similarly, the CCK-8 assay was consistent with the live-dead staining results (Fig. 4B), These results collectively confirm the synergistic anti-tumor advantages of ITD/SA hydrogels through photothermal and chemotherapy, and the addition of ICA could further enhance this effect.

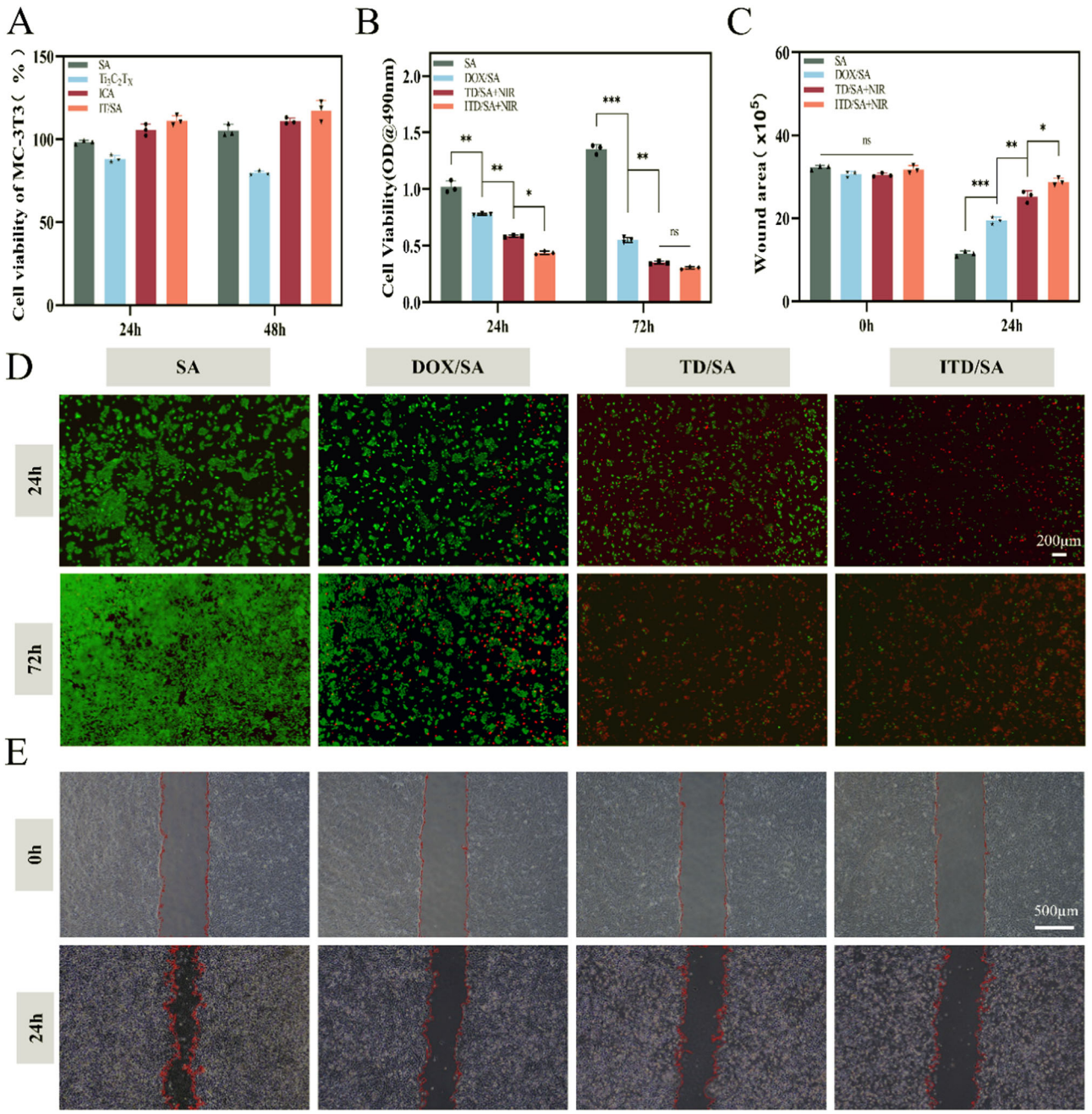

Fig. 4 In Vitro cytotoxicity assays and anti-tumor effects. **A** Cell viability of MC-3T3 cells co-cultured with the materials for 24 and 48 h. **B** CCK-8 assay measuring the cell viability of UMR-106 cells co-incubated with SA, DOX/SA, TD/SA, and ITD/SA hydrogels for 24 and 72 h. **C** Remaining cell migration area at 0 and 24 h. **D** Fluorescence images of UMR-106 cells stained with calcein-AM/PI after co-incubation with SA hydrogel, DOX/SA hydrogel, TD/SA hydrogel, and ITD/SA hydrogel for 24 and 72 h. **E** Scratch assay images of UMR-106 cells co-cultured with hydrogels for 12 and 24 h

3.6 Scratch assay evaluation of hydrogel on UMR-106 Cell migration

The scratch assay (Fig. 4E) demonstrated that the blank area in the DOX/SA, TD/SA, and ITD/SA groups was significantly larger than that in the SA groups. Additionally, it was noted that the DOX/SA, TD/SA, and ITD/SA groups all exhibited varying degrees of cell death and detachment in the unscratched areas, which may be attributed to the cytotoxic effects of DOX alone and in combination with PTT and ICA on tumor cells. By calculating the remaining area, as shown in Fig. 4C, under similar initial conditions, the remaining areas for the SA, DOX/SA, TD/SA, and ITD/SA groups were 11.52, 19.41, 25.24, and 28.79 units after 24 h intervention, respectively.

3.7 Ki67 immunofluorescence staining

Ki67 immunofluorescence staining as shown in Fig. 5A, compared to the SA and DOX/SA groups, there is a significant reduction in green fluorescence in the TD/SA and ITD/SA groups, indicating effective suppression of Ki67 expression. Through quantitative analysis of the average fluorescence intensity, as depicted in Fig. 5B, we found very significant differences in fluorescence intensity, with the DOX/SA, TD/SA, and ITD/SA groups showing 53%, 18% and 9% of the fluorescence intensity of the SA group, respectively.

3.8 Western blot assay

The expression level of related proteins in osteosarcoma cells UMR-106 was examined using the protein blotting technique. As illustrated in Fig. 5C, after 72 h co-culture of tumor cells with TD/SA hydrogel, there was a notable reduction in the expression of PCNA and Bcl-2 proteins, accompanied by a significant increase in Caspase-3 expression. These changes were more pronounced in the ITD/SA group than in the SA, DOX/SA, and TD/SA groups. The level of these protein expressions is quantified and illustrated in Fig. 5D, which correlates with the WB band trend.

3.9 Detoxification effect of ITD/SA on BMSCs

The results are shown in Fig. 6A, the DOX/SA group exhibited a strong red fluorescence, indicating a strong cytotoxic effect on BMSCs. The fluorescence intensity in the TD/SA group displayed a marked reduction compared to the DOX/SA group. Furthermore, the red fluorescence in the ITD/SA group was even fainter than in the TD/SA group, particularly noticeable after 72 h. The CCK-8 assay results in Fig. 6C are consistent with the trends observed in the Live/Dead fluorescence staining, further confirming the advantage of the ITD/SA hydrogel in enhancing therapeutic efficacy while reducing toxicity.

3.10 Osteogenic differentiation of BMSCs

ALP and ARS staining as displayed in Fig. 6B, the SA groups significantly promoted the osteogenic differentiation of BMSCs. Conversely, the DOX/SA group's complete absence of osteogenic differentiation markers suggests that DOX administration might impair the osteogenic differentiation capacity of BMSCs. In contrast, the SA group had the highest staining density, color, and number of mineralized nodules of ALP with ARS nodules among the TD/SA, ITD/SA, and SA groups. This result is confirmed by quantitative analysis of ALP and ARS staining in Fig. 6D.

3.11 Osteogenic fluorescent staining and protein expression

We observed whether ITD/SA hydrogel could salvage the osteogenic differentiation of BMSCs by WB and immunostaining these two genes. The staining results in Fig. 7A, B indicate that both BMP-2 and Runx-2 exhibit intense fluorescence expression in the SA group. In contrast, due to the addition of DOX, the fluorescence levels in the DOX/SA group are extremely low, suggesting that DOX may inhibit the osteogenic differentiation of BMSCs. In the TD/SA and ITD/SA groups, the fluorescence intensity is enhanced due to the incorporation of Ti_3C_2Tx and ICA, although it remains lower than that of the SA group. WB analysis (Fig. 7C, D) demonstrated that the expression of BMP-2 and Runx-2 was most pronounced in the SA group. In the DOX/SA, TD/SA, and ITD/SA groups, the intensity of the blot expression increased sequentially, which is in line with the results we previously obtained through fluorescence staining—signifying that ICA can alleviate the cytotoxic impacts of DOX on BMSCs.

3.12 In vivo anti-tumor and detoxification effects

Given the superior performance of ITD/SA hydrogels in vitro synergistic attenuation and toxicity reduction, in order to determine the feasibility of hydrogel therapy in vivo, we injected appropriate hydrogels into rats with tumors. The course of intervention is shown in Fig. 8A. Among them, the in vivo hydrogel PTT is shown in Fig. 8B. Within 5 min of NIR action, there was a negligible increase in temperature between the SA and DOX/SA groups. However, the temperature in the ITD/SA group increased rapidly, reaching about 43 °C.

Subsequently, we evaluated the anti-tumor effect of this hydrogel by measuring the tumor volume during treatment. As illustrated in Fig. 8C, D, there was a notable increase in tumor volume in the SA group. Compared to the tumors observed in the SA and DOX/SA groups, the tumors in the TD/SA and ITD/SA groups exhibited markedly delayed tumor growth and significantly reduced volumes. Additionally, we monitored the body weight of the rats during the treatment cycle to assess the systemic toxicity of the material. Figure 8E shows that, compared with the SA group, the body weight of the other groups increased uniformly, indicating that the systemic toxicity of the hydrogel may be minimal/non-existent. The results confirm that the ITD/SA hydrogel has strong potential for phototherapy combined with chemotherapy in vivo anti-tumor treatment.

Others, to estimate the improvement of osteogenesis during tumor treatment with ITD/SA hydrogel, HE staining of the femur was performed. Figure 8F shows that the SA group had osteolytic changes in the bone marrow cavity, and the bone defect was further aggravated in the DOX/SA group, indicating the osteogenesis-inhibitory effect of DOX.

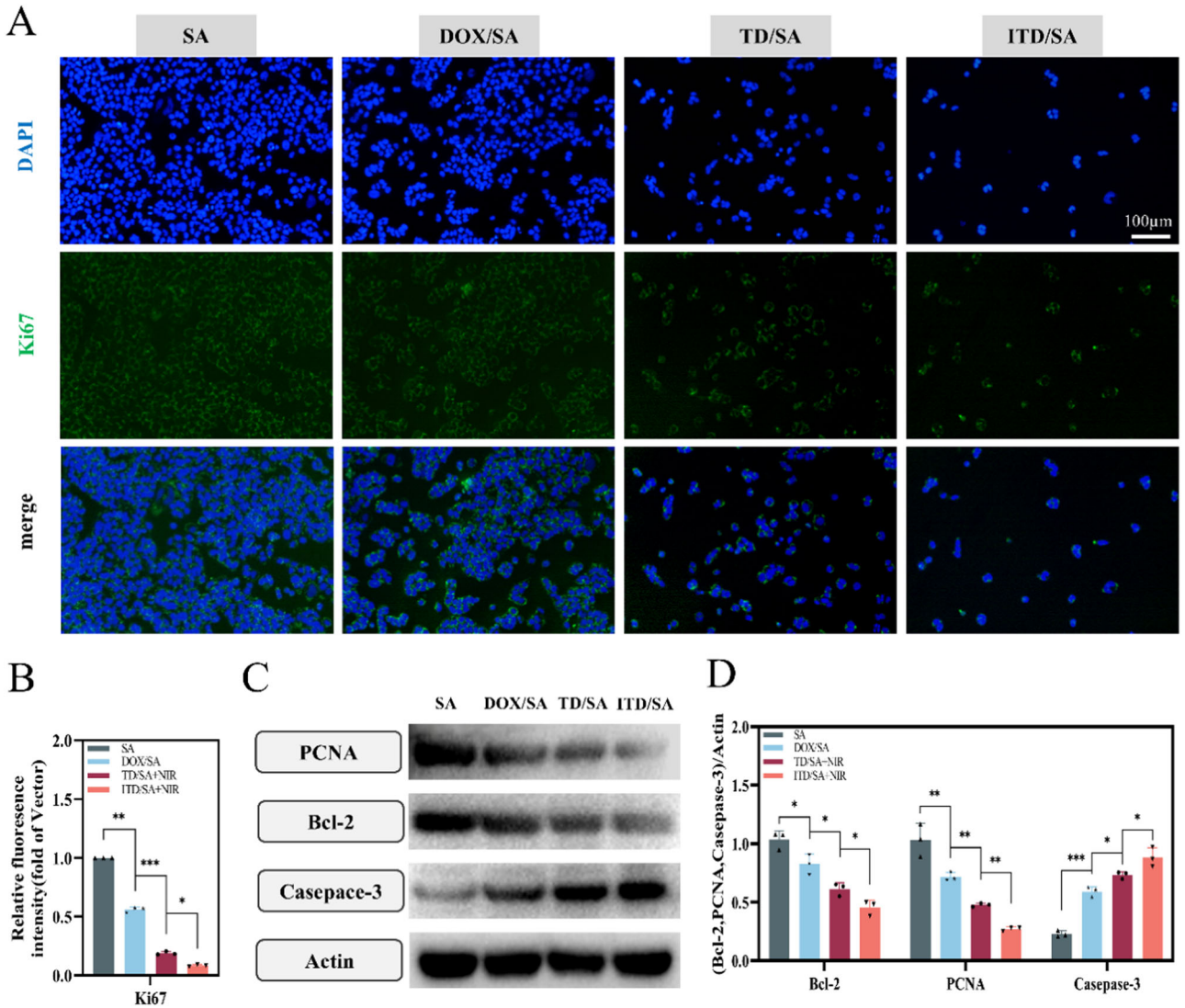

Fig. 5 In vitro fluorescence staining and western blot analysis. **A** Ki67 immunofluorescence staining of UMR-106 cells co-cultured with various hydrogels. **B** Quantitative analysis of Ki67 fluorescence intensity. **C**, **D** Western blot analysis and quantitative analysis of anti-apoptotic proteins (Bcl-2, PCNA) and apoptotic protein (Caspase-3)

Compared to the TD/SA group, the ITD/SA group had better bone repair, indicating that the addition of ICA can reduce the osteogenic inhibition of DOX.

4 Discussion

OS often occurs in the metaphysis of long bones, and the tumor is infiltrative, with obvious bone destruction, often in the form of bone destruction mixed with osteolysis and osteogenesis [29]. OS patients are prone to pathological fractures due to bone destruction. Surgical resection of OS combined with drug treatment is the most common modality at present, but it is associated with high large trauma, long operation time, high risk, and increased risk of postoperative complications [30, 31]. The use of topical hydrogel delivery of DOX for the treatment of OS has been used in a wide range of applications [32–34]. In this study, we prepared an injectable TD/SA hydrogel with the characteristics of minimally invasive, targeted injection, and good biocompatibility and degradation, which has significant advantages in replacing surgical treatment of OS. In addition, the introduction of the photothermal converting agent Ti_3C_2Tx is a combination of phototherapy and chemotherapy. On the one hand, PTT can adjust the intensity of NIR to meet different therapeutic needs. For example, it has been shown that mild photothermal (42–45 °C) has fewer side effects and has great potential in tumor therapy [35]. Similarly, the proliferation of BMSCs is positively affected in an environment around 43 °C [36]; on the other hand, composite hydrogels possess in vitro NIR responsiveness for controlled drug release through Ti_3C_2Tx-mediated

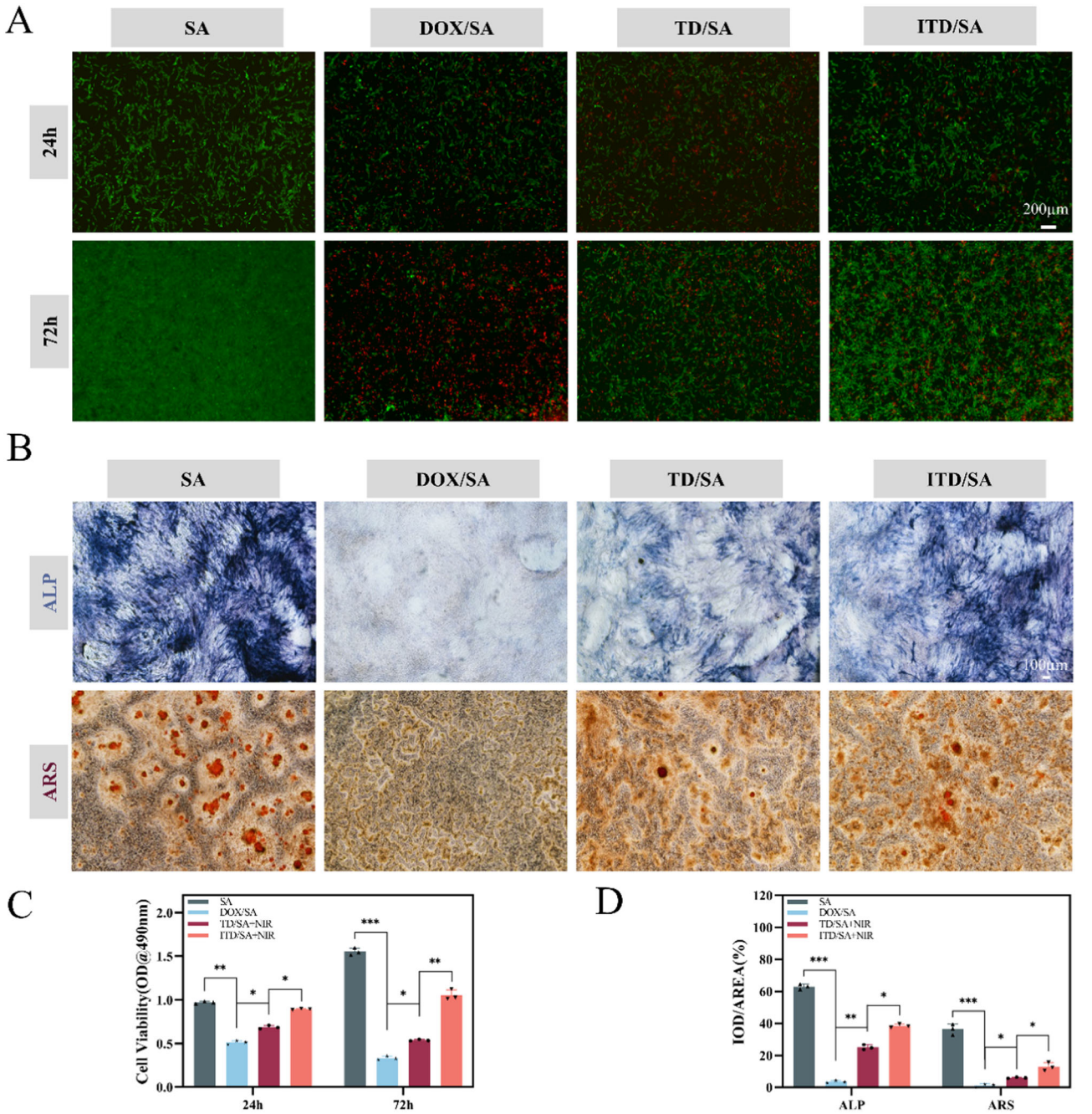

Fig. 6 Effects of hydrogels on BMSCS. **A** Live/dead staining images of BMSCS co-cultured with SA hydrogel, DOX/SA hydrogel, TD/SA hydrogel, and ITD/SA hydrogel for 24 and 72 h. **B** ALP staining images at 7 days and ARS staining images at 14 days. **C** CCK-8 assay measuring cell viability of cells co-incubated with various hydrogel groups for 24 and 72 h. **D** Quantitative analysis of ALP and ARS staining

photothermal modulation. However, it has been shown that DOX has toxic side effects on osteoblasts [37], which may prolong the OS bone healing time/lead to an increased risk of bone non-healing, limiting the use of DOX in restoring function in OS patients.

Summarily, our study introduced the osteoprotective agent ICA to modify the TD/SA hydrogel on this basis, to enhance the anti-tumor properties while attenuating the osteogenic toxicity. First, we observed the characterization of hydrogels loaded with different materials. We found that the ITD/SA composite hydrogels had excellent swelling properties and could achieve rapid solution-gelation changes. The addition of materials only changed the appearance color and did not affect the porosity, injectability, and drug release properties of the hydrogels.

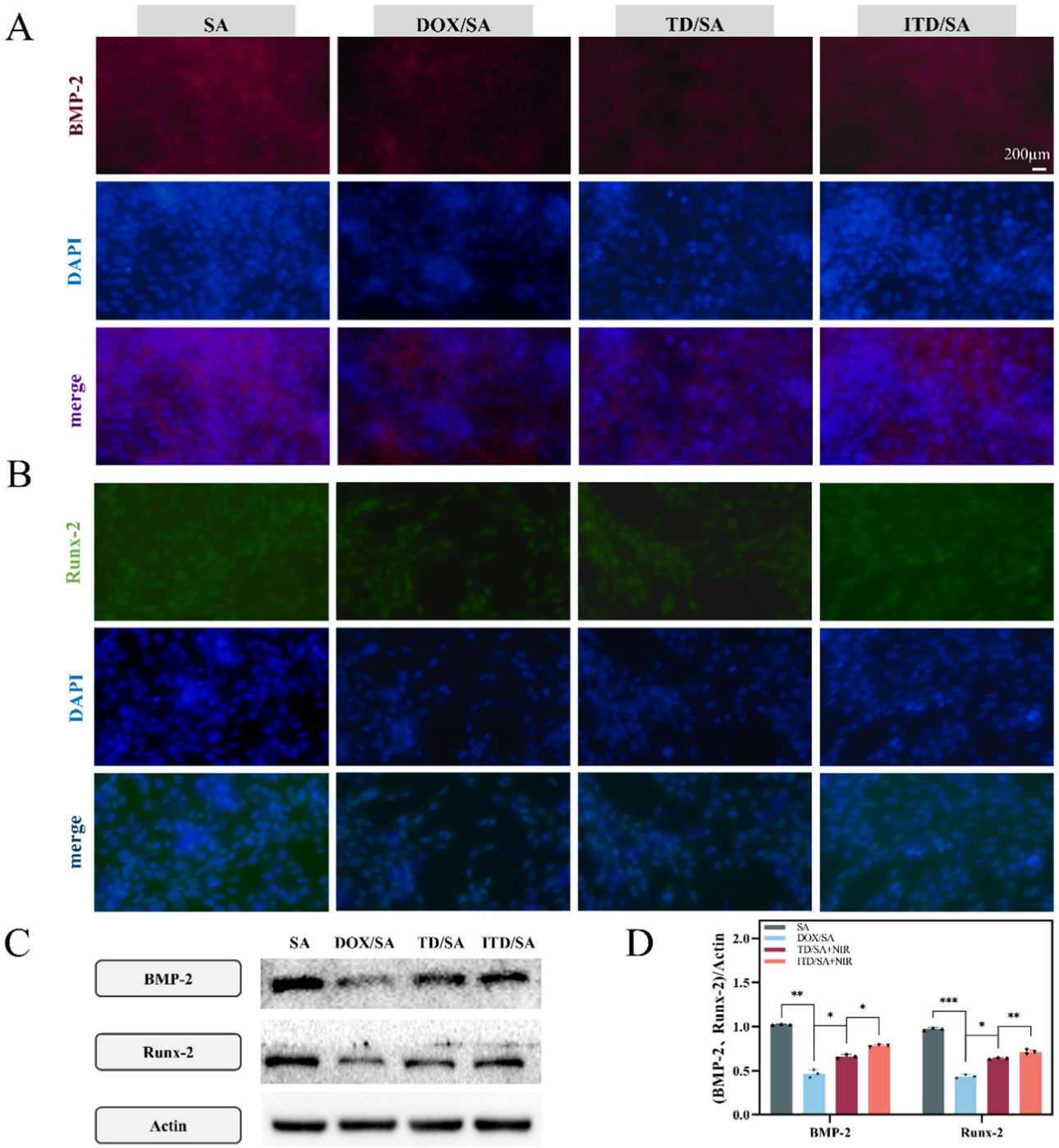

Fig. 7 The role of ITD/SA hydrogel in osteogenic differentiation of BMSCS. **A**, **B** Immunofluorescence staining images of BMP-2 and Runx-2 in BMSCS co-cultured with hydrogels for 72 h. **C**, **D** Western blot analysis and quantitative analysis of osteogenic-related genes (BMP-2, Runx-2)

Migration and invasion are critical properties of many malignant tumors [38]. When ITD/SA hydrogel was co-cultured with UMR-106, the rate of DOX release was significantly increased under NIR irradiation than no NIR irradiation, which combined with the photothermal effect could effectively inhibit the tumor cell viability and migratory ability, and the addition of ICA could further enhance the effect. Ki67 immunofluorescence staining is a technique for detecting a protein marker of the cell cycle in living cells, commonly used in oncology to assess the proliferative capacity of active tumor cells. PCNA is a protein that plays a vital role in the DNA replication process considered an essential cofactor for DNA synthesis, crucial for maintaining the efficiency and accuracy of DNA

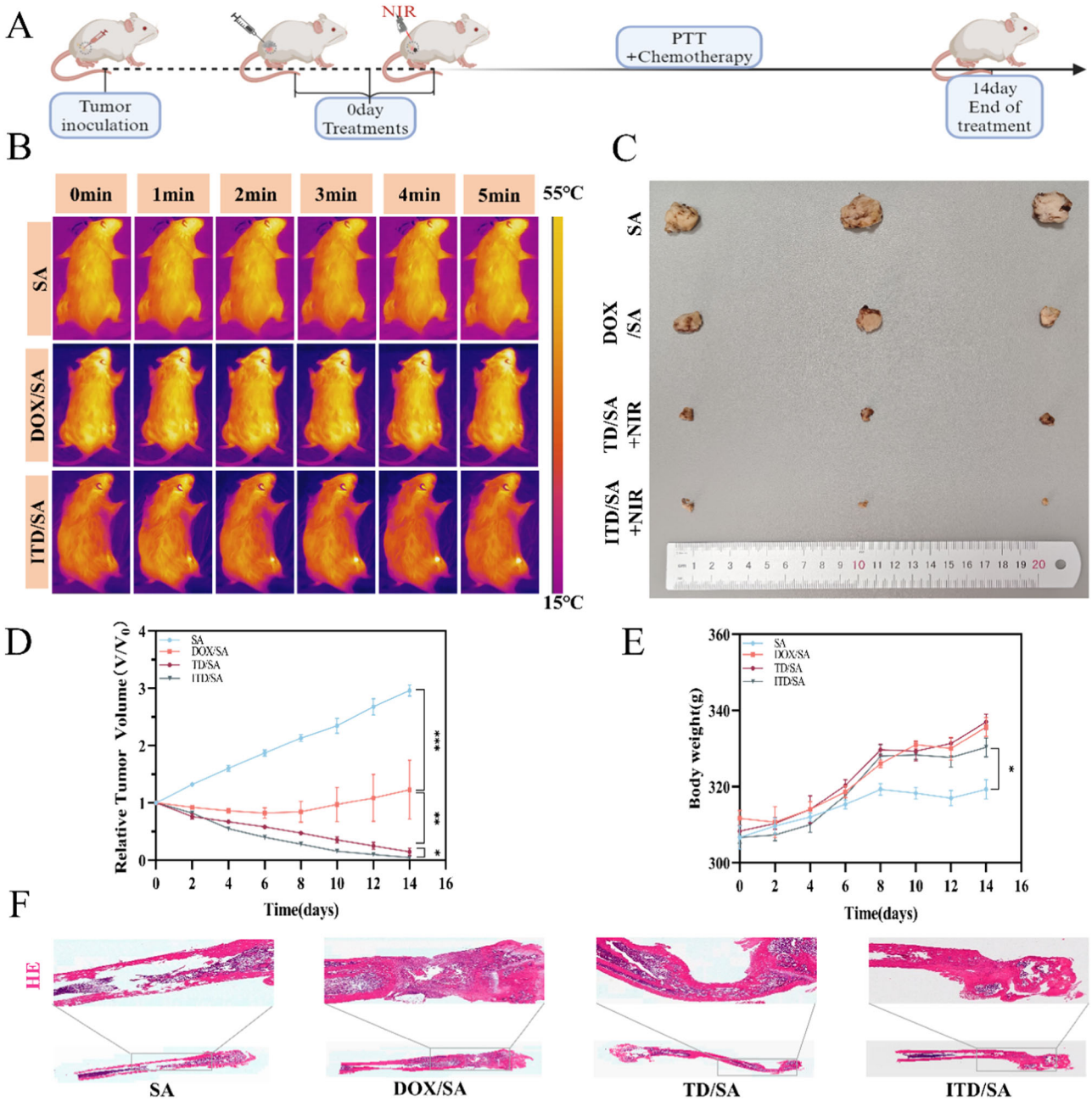

Fig. 8 In vivo anti-tumor effects. **A** Schematic diagram of the treatment cycle. **B** Thermal imaging temperature increase graphs of the SA group, DOX/SA group, and ITD/SA group after NIR (808 nm, 5 min) irradiation. **C** Gross anatomy images of tumor specimens after 14 days of treatment. **D** Relative tumor volume change curve. **E** Changes in rat body weight during treatment. **F** HE staining of the femur. Note: $^{*}P < 0.05$, $^{**}P < 0.01$ and $^{***}P < 0.001$

synthesis. In cancer cells, the expression of PCNA is often increased, reflecting their proliferative potential. The Bcl-2 protein is a critical regulator in the process of cell apoptosis; and its primary function is to inhibit the activity of pro-apoptotic factors, protecting cells from apoptosis. Caspase-3, as a core executor of cell apoptosis, plays an important role in the process of cell apoptosis and is often used as a biological marker of tumor cell apoptosis. Similarly, UMR-106 cells showed a significant decrease in the gene expression of Ki67 and apoptosis-suppressing protein (Bcl-2, PCNA) and a significant increase in the gene expression of pro-apoptosis protein (Caspase-3) after the above treatments, proving the anti-tumor effect of the ITD/SA hydrogel.

BMSCs, with their multidirectional differentiation and self-renewal ability, play an important role in bone repair species [39]. When ITD/SA hydrogel was co-cultured with BMSCs, the survival rate of the ITD/SA group was

significantly increased compared to the killing effect on BMSCs in the DOX/SA group. ALP and ARS are widely recognized markers of osteogenic activity and typical products of osteogenic differentiation [40]. Runx-2 is a specific transcription factor that induces the differentiation and maturation of osteoblasts, and BMP-2 is one of the most significant growth factors [41]. Similarly, the expression of these osteogenesis-related genes (ALP, ARS, Runx-2, and BMP-2) was significantly increased in the ITD/SA group relative to the DOX/SA group, demonstrating that ITD/SA attenuates the osteogenic inhibitory effect of DOX. In vivo experiments in rats also yielded these results. An osteosarcoma model was constructed in the femoral stem of rats using in situ tumorigenesis followed by implantation of ITD/SA hydrogel and application of the corresponding NIR intervention. At the end of the treatment period, it was observed that, on the one hand, the tumor volume of the ITD/SA group was smaller than that of the other groups, indicating a significant anti-tumor effect; on the other hand, in the HE staining of the femur, the bone repair of the ITD/SA group was superior to that of the DOX/SA and TD/SA groups. In conclusion, ITD/SA hydrogel could enhance the anti-tumor effect while attenuating the osteogenic toxicity. In addition, the biosafety of tissue engineering materials is an important factor that should be considered. We demonstrated in both in vivo and ex vivo experiments that this composite hydrogel has good biosafety and has the potential for further in vivo applications.

5 Conclusion

In this study, we designed a multifunctional self-assembled injectable hydrogel system. The ITD/SA composite hydrogel demonstrated rapid gelation speed, favorable photothermal properties, and a high drug-loading capacity. By encapsulating ICA, Ti_3C_2Tx, and DOX in a self-assembled injectable hydrogel, we achieved an excellent anti-tumor effect while reducing the inhibition of osteoblasts by DOX. Irradiation with NIR enabled the photothermal effect of Ti_3C_2Tx to be combined with the sustained release of ICA and DOX, effectively eliminating the tumor. Furthermore, incorporating ICA mitigates DOX's inhibitory impact on the proliferation and differentiation of BMSCs. In vivo experiments have demonstrated that the ITD/SA composite hydrogel system exhibits excellent biocompatibility, a robust anti-tumor effect, and significantly reduced osteogenic toxicity effects. In conclusion, this injectable multifunctional hydrogel based on combined photodynamic and chemodynamic therapy can significantly improve osteosarcoma's therapeutic efficacy while offering a novel approach to mitigate the osteogenic inhibitory effects of DOX.

Supplementary information The online version contains supplementary material available at https://doi.org/10.1007/s10856-025-06874-7.

Acknowledgements This work was supported by the Jiangsu Provincial Medical Key Discipline (Laboratory) (JSDW202252), the National Natural Science Foundation of China (82074471), and the Science and Technology Development Programme Project of Jiangsu Provincial Administration of Traditional Chinese Medicine (MS2023023).

Compliance with ethical standards

Conflict of interest The authors declare no competing interests.

Publisher's note Springer Nature remains neutral with regard to jurisdictional claims in published maps and institutional affiliations.

Abbreviations

T	Ti_3C_2Tx
I	Icariin
D	Doxorubicin
SA	Sodium alginate
CA	Citric acid
NIR	Near-infrared

References

1. Zhou W, Zheng H, Du X, Yang J, Zhou W, Zheng H, et al. Characterization of FGFR signaling pathway as therapeutic targets for sarcoma patients. Cancer Biol Med. 2016;13:260–8.
2. Mizushima E, Tsukahara T, Emori M, Murata K, Akamatsu A, Shibayama Y, et al. Osteosarcoma-initiating cells show high aerobic glycolysis and attenuation of oxidative phosphorylation mediated by LIN28B. Cancer Sci. 2020;111:36–46.
3. Yang Z, Liu J, Lu Y. Doxorubicin and CD-CUR inclusion complex co-loaded in thermosensitive hydrogel PLGA-PEG-PLGA localized administration for osteosarcoma. Int J Oncol. 2020;57:433–44.
4. Simpson EL, Paller AS, Siegfried EC, Boguniewicz M, Sher L, Gooderham MJ, et al. Efficacy and safety of dupilumab in adolescents with uncontrolled moderate to severe atopic dermatitis. JAMA Dermatol. 2020;156:44.
5. Cui H, You Y, Cheng G, Lan Z, Zou K, Mai Q, et al. Advanced materials and technologies for oral diseases. Sci Technol Adv Mater. 2023;24:2156257.

6. Li M, Bu W, Ren J, Li J, Deng L, Gao M, et al. Enhanced synergism of thermo-chemotherapy for liver cancer with magnetothermally responsive nanocarriers. Theranostics. 2018;8:693–709.
7. Kong C, Chen X. Combined photodynamic and photothermal therapy and immunotherapy for cancer treatment: a review. Int J Nanomed. 2022;17:6427–6446.
8. He C, Wang S, Yu Y, Shen H, Zhao Y, Gao H, et al. Advances in biodegradable nanomaterials for photothermal therapy of cancer. Cancer Biol Med. 2016;13:299–312.
9. Wang J, Ma J, Tai Z, Li L, Zhang T, Cheng T, et al. Nanocarrier-mediated immunogenic cell death for melanoma treatment. Int J Nanomed. 2023;18:7149–72.
10. Zhang M, Zhang F, Liu T, Shao P, Duan L, Yan J, et al. Polydopamine nanoparticles camoufaged by stem cell membranes for synergistic chemo-photothermal therapy of malignant bone tumors. Int J Nanomed. 2020;15:10183–97.
11. Wang M, Wang Y, Fu Q. Magneto-optical nanosystems for tumor multimodal imaging and therapy in-vivo. Mater Today Bio. 2024;26:101027.
12. Chen Y, Xu J, Li P, Shi L, Zhang S, Guo Q, et al. Advances in the use of local anesthetic extended-release systems in pain management. Drug Deliv. 2024;31:2296349.
13. Cai R, Xiao L, Liu M, Du F, Wang Z. Recent advances in functional carbon quantum dots for antitumour. Int J Nanomed. 2021;16:7195–229.
14. Wang Z, Geest ICVD, Leeuwenburgh SC, van den Beucken JJ. Bifunctional bone substitute materials for bone defect treatment after bone tumor resection. Mater Today Bio. 2023;23:100889.
15. Li X, Wang Y, Liu T, Zhang Y, Wang C, Xie B. Ultrasmall graphene oxide for combination of enhanced chemotherapy and photothermal therapy of breast cancer. Colloids Surf. B Biointerfaces. 2023;225:113288.
16. Li S, Qing Y, Lou Y, Li R, Wang H, Wang X, et al. Injectable thermosensitive black phosphorus nanosheet- and doxorubicin-loaded hydrogel for synergistic bone tumor photothermal-chemotherapy and osteogenesis enhancement. Int J Biol Macromol. 2023;239:124209.
17. Zeng G, Chen Y. Surface modification of black phosphorus-based nanomaterials in biomedical applications: strategies and recent advances. Acta Biomater. 2020;118:1–17.
18. Zhang Y, Qu X, Zhu C, Yang H, Lu C, Wang W, et al. A stable quaternized chitosan-black phosphorus nanocomposite for synergetic disinfection of antibiotic-resistant pathogens. ACS Appl Bio Mater. 2021;4:4821–32.
19. Cui J, Peng Q, Zhou J, Sun Z. Strain-tunable electronic structures and optical properties of semiconducting MXenes. Nanotechnology. 2019;30:345205.
20. Li R, Zhang L, Shi L, Wang P. MXene Ti_3C_2: an effective 2D light-to-heat conversion material. ACS Nano. 2017;11:3752–9.
21. Abd El-Ghaffar MA, Hashem MS, El-Awady MK, Rabie AM. pH-sensitive sodium alginate hydrogels for riboflavin controlled release. Carbohydr Polym. 2012;89:667–75.
22. Rashidzadeh B, Shokri E, Mahdavinia GR, Moradi R, Mohamadi-Aghdam S, Abdi S. Preparation and characterization of antibacterial magnetic-/pH-sensitive alginate/Ag/Fe3O4 hydrogel beads for controlled drug release. Int J Biol Macromol. 2020;154:134–41.
23. Tanwar M, Rani A, Gautam N, Talegaonkar S, Gupta RK. Essential oils loaded carboxymethylated Cassia fistula gum-based novel hydrogel films for wound healing. Int J Biol Macromol. 2024;278:134682.
24. Wang Z, Yang L, Xia Y, Guo C, Kong L, Department ONMC, et al. Icariin enhances cytotoxicity of doxorubicin in human multidrug-resistant osteosarcoma cells by inhibition of ABCB1 and down-regulation of the PI3K/Akt pathway. Biol Pharm Bull. 2015;38:277–84.
25. Zhang X, Liu T, Huang Y, Wismeijer D, Liu Y. Icariin: does it have an osteoinductive potential for bone tissue engineering? Phytother Res. 2014;28:498–509.
26. Zhao J, Ohba S, Komiyama Y, Shinkai M, Chung U, Nagamune T. Icariin: a potential osteoinductive compound for bone tissue engineering. Tissue Eng Part A. 2010;16:233–43.
27. Yu Z, Sun H, Fan Q, Long H, Yang T, Ma B. Establishment of reproducible osteosarcoma rat model using orthotopic implantation technique. Oncol Rep. 2009;21:1175.
28. WARE JL, DeLong ER. Influence of tumour size on human prostate tumour metastasis in athymic nude mice. Br J Cancer.1985;51:419–23.
29. Cascini C, Chiodoni C. The immune landscape of osteosarcoma: implications for prognosis and treatment response. Cells. 2021;10:1668.
30. Gonzalez MR, Karczewski D, Bedi ADS, Denwood H, Lozano Calderon SA. Risk factors for 30-day soft tissue complications after pelvic sarcoma surgery: a National Surgical Quality Improvement Program study. J Surg Oncol. 2023;128:367–74.
31. Bensaid S, Contejean A, Morand P, Enser M, Eyrolle L, Charlier C, et al. Surgical site infection after pelvic bone and soft tissue sarcoma resection: risk factors, microbiology, and impact of extended postoperative antibiotic prophylaxis. J Surg Oncol. 2023;128:344–9.
32. Si M, Xia Y, Cong M, Wang D, Hou Y, Ma H. In situ co-delivery of doxorubicin and cisplatin by injectable thermosensitive hydrogels for enhanced osteosarcoma treatment. Int J Nanomed. 2022;17:1309–22.
33. Ma H, He C, Cheng Y, Yang Z, Zang J, Liu J, et al. Localized co-delivery of doxorubicin, cisplatin, and methotrexate by thermosensitive hydrogels for enhanced osteosarcoma treatment. ACS Appl Mater Interfaces. 2015;7:27040–8.
34. Li K, Zhao D, Chen H, Zhang W, Zhao W, Zhang Z. Thermosensitive hydrogel-mediated locally sequential release of doxorubicin and palbociclib for chemo-immunotherapy of osteosarcoma. Mater Design. 2022;224:111365.
35. He X, Zhang S, Tian Y, Cheng W, Jing H. Research progress of nanomedicine-based mild photothermal therapy in tumor. Int J Nanomed. 2023;18:1433–68.
36. Zhang J, Tang S, Ding N, Ma P, Zhang Z. Surface-modified Ti(3) C(2) MXene nanosheets for mesenchymal stem cell osteogenic differentiation via photothermal conversion. Nanoscale Adv. 2023;5:2921–32.
37. Banerjee D, Bose S. Comparative effects of controlled release of sodium bicarbonate and doxorubicin on osteoblast and osteosarcoma cell viability. Mater Today Chem. 2019;12:200–8.
38. Zhang LN, Zhang DD, Yang L, Gu YX, Zuo QP, Wang HY, et al. Roles of cell fusion between mesenchymal stromal/stem cells and malignant cells in tumor growth and metastasis. FEBS J. 2021;288:1447–56.
39. Arthur A, Gronthos S. Clinical application of bone marrow mesenchymal stem/stromal cells to repair skeletal tissue. Int J Mol Sci. 2020;21:9759.
40. Tong L, Liao Q, Zhao Y, Huang H, Gao A, Zhang W, et al. Near-infrared light control of bone regeneration with biodegradable photothermal osteoimplant. Biomaterials. 2019;193:1–11.
41. Huang K, Wu J, Gu Z. Black phosphorus hydrogel scaffolds enhance bone regeneration via a sustained supply of calcium-free phosphorus. ACS Appl Mater Interfaces. 2019;11:2908–16.